The Pennsylvania State University

The Graduate School

STUDY OF PROCESS-STRUCTURE-PROPERTY RELATIONSHIPS IN STAINLESS STEEL 316L MADE BY POWDER BED FUSION

A Thesis in

Additive Manufacturing and Design

by

John O'Brien

Submitted in Partial Fulfillment
of the Requirements
for the Degree of

Master of Science
December 2020

The thesis of John O'Brien was reviewed and approved by the following:

Allison Beese
Associate Professor of Materials Science and Engineering and Mechanical Engineering
Thesis Co-Adviser

Timothy W. Simpson
Paul Morrow Professor of Engineering Design & Manufacturing
Thesis Co-Adviser
Program Chair, Additive Manufacturing and Design

Guha Manogharan
Assistant Professor of Mechanical and Nuclear Engineering

Abstract

This thesis aims to identify important links in the process-structure-property relationships in 316L Stainless Steel manufactured by laser powder bed fusion (L-PBF) additive manufacturing. The ultimate aim is to generate a model that can predict mechanical properties, including Ultimate tensile strength, based on laser power, scan speed, and hatch spacing parameter settings for the L-PBF process. The relationship between these parameters, microstructural features, and mechanical properties is investigated using the Advanced data SCiENce toolkit for Non-Data Scientists (ASCENDS). The microstructure of the built parts was examined using electron backscatter diffraction in order to quantify grain sizes, crystallographic orientations of grains, and grain morphologies. The length scale of the cellular solidification structure, on the order of 0.5-1 um, was also investigated as this relates to both volumetric energy density input and strength. Scanning electron microscopy was used to measure the size of the solidification cells. It was found that the interplay between these three process parameters is more complex than initially anticipated, and multi-variable experimentation failed to produce a useful predictive model. However, important links between microstructural features and process parameters were established, providing an increased understanding of the impacts of laser power, scan speed, and hatch spacing on grains and solidification cells.

Contents

List of Tables

List of Figures

Acknowledgments

The authors would like to acknowledge the Office of Naval Research and Senvol through grant number 205455. Any opinions, findings, and conclusions or recommendations expressed in this publication are those of the authors and do not necessarily reflect the views of the Office of Naval Research or Senvol.

Additionally, I would like to thank Dr. Allison Beese and Dr. Time Simpson for advising my through the course of this project. Their advice has proved invaluable and I am better for having worked with them. I would also like to thank the members of the Beese research group for their advice and support.

Finally, I would like to thank the staff at the Materials Characterization lab for their help in getting experience on the electron microscopses, and helping me work through any and all of the issues I had when preparing samples for EBSD.

1. Chapter 1: Introduction

1.1. Additive manufacturing

Additive manufacturing, also known as 3D printing, is an important new technology, one that presents opportunities to improve products and industrial processes. Additive manufacturing encompasses a large set of technologies, including the manufacture of parts of metal, ceramic, or polymer through a wide variety of processing routes, most commonly in a layer-by-layer deposition. Figure 1 provides an overview of a number of processing routes for additively manufacturing metallic parts. The fundamental basis of these technologies is the addition of material to some form of a substrate or platform in order to "build up" material to reach the final shape. This layerwise fabrication allows for the creation of shapes that may otherwise generate large amounts of waste when made through traditional subtractive machining processes. These technologies are used with a variety of feedstocks to create a large variety of products [1].

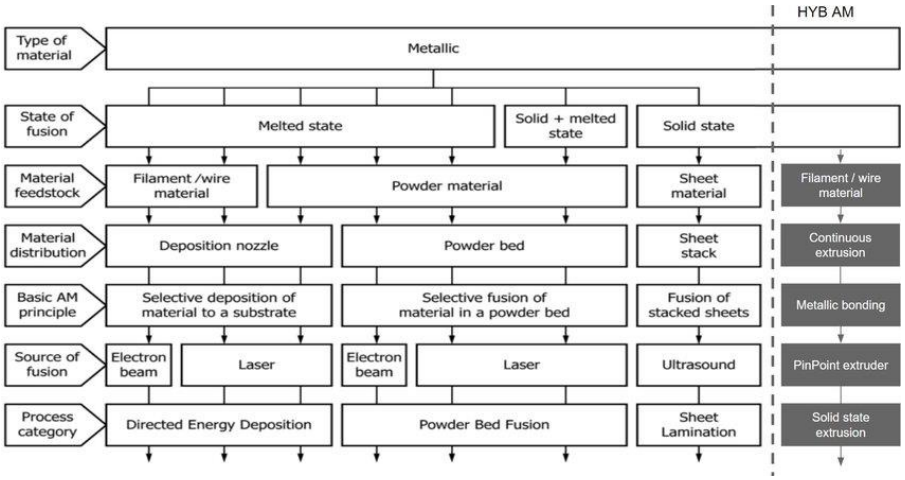

Figure 1. Showcasing the wide variety of additive manufacturing techniques. Adapted from ISO/ASTM 52900

One of the additive manufacturing technologies of great use to industry is laser powder bed fusion (L-PBF). This technology uses a high-intensity laser, scanned across the surface of a powder bed, to selectively melt the material. The laser is focused to a spot on the bed with

controllable diameter, commonly on the order of 100 μm [2]. It is scanned across the bed, and after the processing of one layer, the bed and substrate are lowered, and the process is repeated.

With this technology, it is possible to make unit runs of a single part cost-effectively, allowing parts or geometries that are optimized according to their service conditions and free from traditional production-related constraints. This is particularly suited to the production of small-batches, weight reduction, part customization, and functional integration.

As the laser beam creates an extremely small melt pool within the focal spot, a measure of energy density is used in the quantitative evaluation of process parameters and bulk properties. Energy density is commonly defined in two ways. Linear energy density is given as

$$E_l = \frac{P_l}{v_l} \qquad \text{Eq (1)}$$

where the laser power, P_l, is divided by the scan speed of the laser, v_l. Important to note is that linear energy density disregards hatch spacing, the space between laser weld tracks as well as the thickness of the deposited powder layer.

Volumetric energy density is given as

$$E_v = \frac{P_l}{V_l * S_h * T_l} \qquad \text{Eq (2)}$$

where P_l is the laser power divided by the product of scan speed of the laser, V_l, hatch spacing S_h, and layer thickness T_l. Volumetric energy density takes into account the layer thickness, however, in L-PBF, it is necessary to melt through multiple layers, in order to form metallurgical bonds. Linear energy density and volumetric energy capture this differently. And may capture properties differently in different material systems.

In L-PBF, the objective is to selectively melt and densify metal powder, layer by layer, in order to form a finished part. Fundamentally, this melting and densification require two things: first, the complete melting of powder particles where the laser is scanned. Second, the partial

melting of the *prior layer* is required in order to form a metallurgical bond between the layers [1]. This clearly establishes a minimum threshold for energy being put into the system.

While it is less clearly defined, there is also a maximum threshold for work put into the system. As metals have a melting point, they have a boiling point where vaporization occurs. While reaching the energy density needed to vaporize metal is uncommon in traditional metallurgical forming processes like investment casting or forging, it is easily achievable in L-PBF [3]. This vaporization will introduce keyhole defects when it occurs, an example of which is shown in Figure 2 [4]. A practical ceiling for energy density is one that minimizes the formation of vaporization-related defects. While it is possible to always tune the parameter set to the low end of the spectrum of permissible energy densities, the tradeoff will be a loss in productivity, as a lower energy density will require more "time on target" for the laser to achieve complete melting.

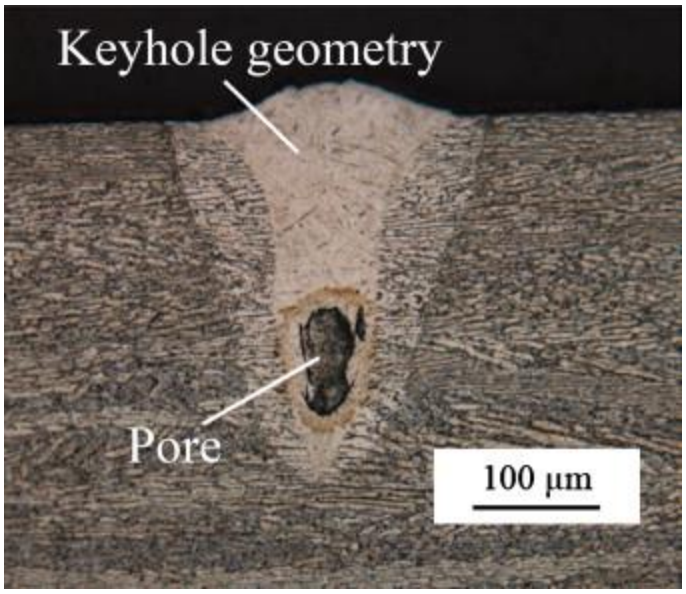

Figure 2. Deliberately generated keyhole pore. This artifact is created as a result of vaporization and the influence of that gas pressure on the melt pool [4].

With the energy density (ED) as an important parameter in the process of L-PBF, the two ways of quantifying ED have a material impact on the understanding of the process. In this work, the correlation between linear and volumetric energy densities is investigated as they relate to the mechanical properties and microstructure.

1.2.Laser-based powder bed fusion

The manufacturing of objects via laser powder bed fusion is done in a stepwise fashion: a layer of powder is deposited, a high-powered laser scans across the surface of the powder, selectively melting, creating metallurgical bonding within the layer and to prior layers. This results in the final part resembling a collection of micro-welds that are all bonded together. A representation of L-PBF working principle is shown in Figure 3, and the overall process can be summarized as follows:

1) First, CAD manipulation and model “slicing” occur, the latter being performed by specific software that subdivides the geometry into slices with a defined thickness according to the target layer height.
2) Then, data is loaded into the L-PBF print system, containing the powder, the laser, and all associated systems.
3) Next, production of the part via L-PBF occurs:
    a) First, the powder is spread across the build area with a rake, wiper, or roller (the leveling system indicated in Figure 3).
    b) Then, the laser is switched on and scanned across the surface in a controlled manner, selectively melting the metal powder that was spread in Step a.
    c) After the slice of the geometry is melted, the build platform is lowered by the indicated layer height.

d) Steps 3a–3c are repeated until all layers are fused.

4) After the entire height of the part has been solidified, the unused powder is removed, and the final part is extracted from the build volume.

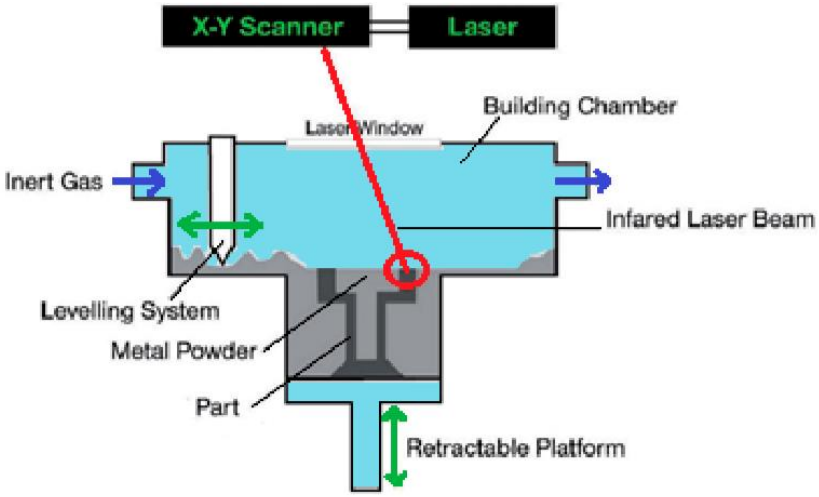

Figure 3. Schematics of a generic laser powder bed fusion system [6]

1.3.Material selection for additive manufacturing

Nominally, every material that can be welded can be processed via a laser powder bed fusion route, provided the proper processing parameters are developed [5]. However, due to costs related to the AM process, it is the focus of many working groups to develop the technology for two often overlapping classes of materials: (i) ones that are of particular interest in engineering due to their wide range of applications and (ii) ones that are difficult to process by other means.

A material that is commonly used in the AM process is 316L stainless steel, an austenitic stainless steel, with the primary alloying elements nickel and chrome, at 10 and 18 weight percent, respectively. These elements contribute to the material's excellent corrosion resistance. However, they also drive a relatively low AISI machinability index of 0.45, on a scale of 0 to 1, with 1 being free machining [6]. In 316L, the "L" indicates a carbon content lower than 0.03%, which contributes to good weldability. The combination of difficult subtractive manufacturing,

good mechanical strength, corrosion resistance, and weldability makes 316L an optimal grade for L-PBF [7].

Of interest to industry is the ability to evaluate the mechanical properties of an alloy without mechanical testing, as mechanical testing is a long and expensive process, requiring a number of secondary operations, additional equipment, and trained staff. This project aims to use a combination of techniques to evaluate the mechanical properties of the 316L stainless steel and develop links between structure, processing, and properties.

1.4. 316L Stainless Steel

316L stainless steel is an austenitic stainless steel, with the composition listed in Table 1. The primary alloying elements are Nickel and Chrome, and the L designation indicates a carbon content of less than 0.03%. These alloying elements provide good mechanical properties as well as good corrosion resistance, particularly against chloride corrosion. This makes 316L an extremely popular application for marine and construction applications. Additionally, these provide for mechanical and corrosion properties that are maintained at elevated temperatures.

Table 1. Chemical composition of 316L stainless steel used in this work. Composition given as weight percent.

Fe	Balance
Cr	18.30
Ni	13.18
Mo	2.46
Mn	0.4
C	0.02

316L is a fully austenitic from room temperature to the melting point due to the stabilizing effect of Ni (at contents over 12%). While it is possible to form a sigma phase in 316L that will negatively affect the material properties, the formation of the sigma phase has unfavorable enough kinetics to be nearly entirely avoided in the AM process [8]. As a result, 316L will receive limited benefit from heat treatment as there are no precipitates or secondary phases that can be controlled in order to modify the mechanical properties. In most cases, post-build heat treatment will be limited to the relief of residual stresses, which occur as a result of the rapid solidification in the L-PBF process [9].

1.5.L-PBF processing parameters

The L-PBF process involves an extremely small molten region, with a diameter ranging from 50 to 100 μm and the interaction of this small melt pool with small metal powder particles, which exist on a similar length scale[1] [10]. This interaction of melt pool and unmelted particles occurs next to the comparatively vast heat sinks of the build plate and manufactured bulk. This juxtaposition of small melt pools and vast cooling potential leads to rapid solidification of the melt, with cooling rates approaching 10^7 K/s [11]. A consequence of this is that the laser and

scan parameters used in the building of the part have a significant impact on the final properties of the part as it is produced. There are considered to be three groups of process parameters of varying controllability by the user.

1) Machine parameters
    a) Scan pattern
    b) Laser power
    c) Scan speed
    d) Layer thickness
2) Powder bed parameters
    a) Powder bed packing density
    b) Build chamber gas composition
    c) Build chamber gas flow
    d) Build plate temperature
3) Powder parameters
    a) Sphericity
    b) Particle size distribution
    c) Flowability
    d) Chemical composition

All of these parameters can have an impact on the mechanical properties of the as-built part [12]. After the build is complete, other processing steps, namely, surface or heat treatments, can be taken to modify final properties. However, it is important to note that AM processes where melting occurs are effectively producing the alloy and the geometry simultaneously, so any microstructure scale defects will directly impact the performance of the final part. Machine

parameters are the most easily controlled in the AM process; so, there is a large reliance on the optimization of machine parameters in order to produce the mechanical properties necessary in the final part. The impacts of different machine parameters are discussed next.

1.5.1. Machine Parameters

Scan pattern

While not a parameter that is explicitly user-defined at the L-PBF machine, the scan pattern can have a significant effect on the resulting part. Scan pattern refers to the path that the laser spot follows over the surface of the part to be selectively melted. As there is an extreme thermal gradient in the immediate vicinity of the melt pool, the scan strategy can have an influence on that thermal gradient. As residual stresses are related to thermal gradients upon solidification, the choice of scan strategy can have an influence on mechanical properties, including the residual stresses contained in the build [13].

Choo et al. [13] investigated the effects of laser power on the number of defects and the texture of additively manufactured 316L stainless steel. This was done with a laser power ranging from 200W to 380W, and a constant scan sped of 300mm/s, resulting in a range of linear energy densities from 0.666J mm^{-1} to 1.26 J mm^{-1}. After the samples were built, they were investigated using synchrotron X-Ray computed microtomography, and it was found that the degree of porosity increased linearly with a decrease in laser power, to a maximum porosity of 0.88%. Additionally, links between laser power and cell spacing were investigated. It was found that as the laser power decreased, the cell size and texture also decreased, indicating that the laser power has a strong effect on cell size and crystallographic texturing.

Laser power

Most L-PBF systems use a laser in the 200 to 1000 watt range. This laser is the fundamental energy source for the AM and melting process. This laser is commonly an Nd-YAG fiber laser, which is operated in such a way as to provide a continuous beam while in operation. There are AM systems that use a pulsed laser for the melting process (e.g., Renishaw's L-PBF systems), but how the different modes impacts the final part is outside the scope of this report.

Irrinki et al. [14] investigated the effects of laser power variations on the densification of 17-4 PH stainless steel. By varying the energy density at the melt pool, different levels of densification were achieved. This is hypothesized to occur as a result of lower viscosities in a melt pool with a higher temperature. As the viscosity of the melt pool decreases, the wetting potential of the melt increases, leading to greater and more uniform densification. At an energy density of 104 J mm^{-3}, the percentage of theoretical density reached was between 96% and 97.5%. In contrast, at 64 J mm^{-3}, the theoretical density ranged from 87% to 97% [14].

Scan speed

The scanning of the laser is typically controlled by a mechanical galvanometer, which "steers" the laser melt pool across the surface of the powder bed. This operates in the 100-1000 mm/s region. The combination of laser power and scan speed is the primary driving force on determining the melt pool characteristics. The combination of laser power and scan speed is often referred to as "linear energy density" per Eq. (1) and is a proxy for specific energy put in to melt the powder bed. As linear energy density decreases, it is possible to observe different defects in the part, post melting. It is also possible to observe defects from energy density being too high. There is an optimal value for a linear energy density that is both material properties dependent and relative to the goal of the process.

Defects that result from too high energy input:

a. Gas entrapment – turbulence in the melt pool may lead to bubbles of gas becoming trapped in the melt as it solidifies.
b. Keyhole porosity – an excessively deep meltpool enables a “pinching off” of void formed by pressure on the liquid

Defects that result from a low energy input:

a. Lack of fusion – insufficient energy results in powder particles not melting
b. Balling – inconsistent meltpool formation leads to the formation of balls of melted material

Layer thickness

Layer thickness is an additional machine parameter that is one of the constants that is used. The powder bed apparatus, as shown in Figure 3, relies on dropping the bed a set amount, and then adding another layer of powder on top. The amount that the bed drops, the layer thickness, has a strong impact on the overall built time and can impact the printing resolution. As the bed drops a larger amount, it is necessary to have a higher linear energy density in order to ensure that the layer of powder is thoroughly melted in a way that the prior layer forms a metallurgical bond with the next layer.

1.5.2. Powder bed parameters

Powder bed packing density

Irrinki et al. [14] showed that there was an impact on the density of the powder bed on the mechanical properties of the finished parts by comparing the mechanical properties of parts built using water atomized and gas atomized powders. Due to atomization mechanics, gas atomized powder particles are more spherical and can be more flowable. Water atomized

powders, with a lower apparent density, showed a lower overall set of mechanical properties, due to a lower part density. Packing density in the powder bed of the machine is not something that is adjusted as a matter of course. Different machine manufacturers will use different methods for spreading powder on a powder bed, with some using a rigid recoater, some using a flexible recoater, and some using a rolling recoater [15].

Build chamber gas composition

In the process of an L-PBF build, a constant gas flow is streamed over the build surface. This gas flow is designed to remove any spatter or fumes that are created during the melting of the metal powder. This may be an oxide layer on the particles themselves or adsorbed organics. Additionally, due to the extremely high specific energy input at the focal point, an alloy with low melting temperature constituents may see those components vaporize. High-velocity gas flow over the surface of the bed is used to mitigate "downstream" effects and clear the build chamber.

Pauzon [16] studied the effects of carrier gas composition on two different alloy systems, 316L and Ti-6Al-4V. It was found that a significant factor in carrier gasses is a need to minimize oxygen content, generally to below 1000ppm, although different alloys have different sensitivities. A change from Argon or nitrogen to a helium blend was found to positively impact the density of the finished part. This is speculated to be a result of the different densities of the gasses, and their capabilities to "knock" detritus out of the build volume [16].

1.6. Microstructure

1.6.1. Grain size and mechanical properties

Other work has investigated the effects of L-PBF process parameters on the microstructure of the resultant L-PBF build. Li et al. [17] found that the contribution of grain boundaries, as defined by the Hall-Petch relationship, was less than 50% of measured

engineering yield strength. Additionally, in the course of investigating solidification structures, Bertoli et al. [18] provided qualitative insight into the effects of scan parameters on microstructure. Figure 4 shows the results of the effects of scan parameters on microstructure, with a linear energy density of 2.0 J/mm used for the left sample and 0.15 J/mm for the sample on the right. This qualitatively shows a significant difference in microstructure as the process parameters are varied. Additionally, in mechanical testing, there was the highest engineering yield strength as well as elongation in the sample processed with the linear energy density of 2.0 J/mm [19].

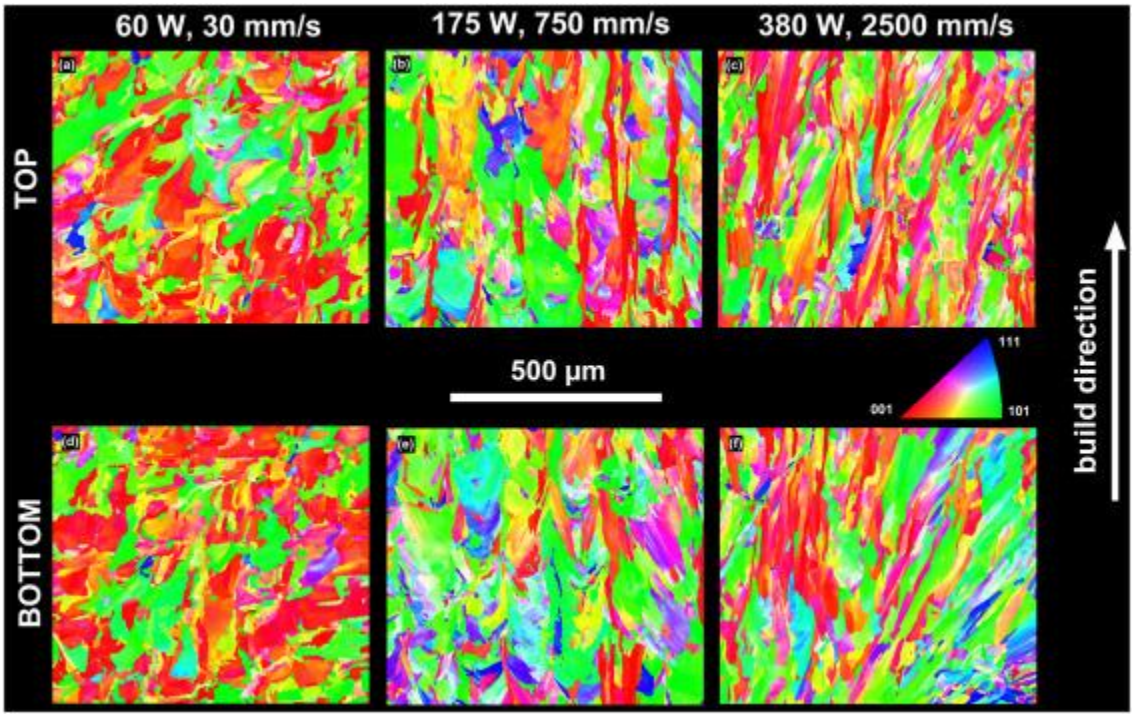

Figure 4. Different microstructures as resulting from different sets of scan parameters.

1.6.2. Solidification cells and mechanical properties

Bertoli et al. [19] investigated the effects of scan parameters on subgranular solidification structures in additively manufactured L-PBF 316L. As the solidification cell formation is a function of temperature gradient and cooling rate, Rosenthal solutions for each of the sets of scan

parameters were calculated [1]. It was found that the Rosenthal solutions for temperature gradient and cooling rate varied little with changes in scan parameters. As such, attempts to modify the solidification structures with manipulation of laser scan parameters were ineffectual in changing the morphologies of the solidification cells.

1.7.Machine learning

Of great interest in nearly every field of study right now is the application of machine learning in order to gain insight into patterns that may exist but in a way that is not readily apparent to human observers, or to automate tasks [20]. Machine learning encompasses a wide variety of techniques and methods, optimized for various tasks. Fundamentally, the field of machine learning is the development of tools that enable computers to perform tasks without explicitly being programmed to do so [21]. A common approach to the problem of machine learning is that of a neural network, such as the example shown in Figure 5.

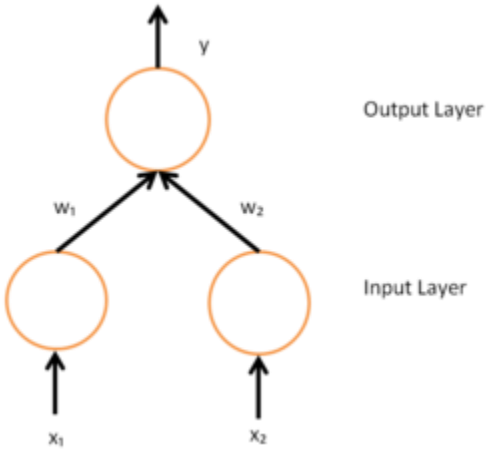

Figure 5. A simple neural network with two input units (each with a single input) and one output unit (with two inputs). [17]

Figure 5 shows a straightforward neural network with two layers: (1) an input layer and (2) an output layer. Two values are passed as inputs to this network, combined linearly, and then that value is used in an activation function to assign a binary response to the inputs.

Fundamentally the use of neural networks involves training data to a machine learning algorithm. This data uses a known set of inputs and outputs in order to arrive at the weights w_1 through w_n for each layer of the neural network. In the example in Figure 5, the two inputs are each weighted and then combined in the output layer, as $y = \frac{1}{1+e^{-(x_1 w_1 + x_2 w_2)}}$. This function, the sigmoid function, returns a value between 0 and 1 for any combination of inputs. However, this combination of functions does not represent all possible logistical functions – it is impossible to train it to mimic an XOR function [22].

In order to ensure that the network is accurate, a backpropagation algorithm is used. The original technique was published in 1986 by Rumelhart, et al. [22]. Backpropagation uses the known inputs and outputs in order to arrive at optimal weights for the neurons. This is done by running known-good values through the neural network "backward." The values output by the neural network are then compared to known good values. The error between the two values is calculated. By a method of gradient descent, the weights are iteratively adjusted to arrive at a minimum error. The example in Figure 5 uses three "neurons," but in commercial deployments, the networks may be much larger, comprising hundreds of thousands or millions of neurons.

This application of test data to the "neural network" is the essence of modern machine learning. As the network is "self-correcting" via the backpropagation method, it can be adapted to many situations. However, as previously mentioned, the correct application of the backpropagation algorithm requires training data [22].

DeCost et al. [23] have deployed a machine learning method in order to develop an algorithm that can identify microstructures with no prior knowledge of the metallurgical features (grain size, grain boundaries, grain morphologies, and secondary phases). This was enabled by an extensive database of pre-labeled micrographs, which were used as the training set. By using a neural network that was trained to develop nonlinear correlations between features in the image and the label of the image, the algorithm was able to classify a novel microstructure with over 80% accuracy.

This result presents an interesting tool but introduces several complications. Any microstructure relationships extracted using this approach are likely to be empirical in nature and correlative rather than causative due to a lack of physically informed correlations. Additionally, machine learning techniques are inherently statistical in nature, thus require any image or dataset to not exhibit too great of a variance from the training dataset. Additionally, modern machine learning techniques are tailored to "web-scale" data, datasets with hundreds of thousands to billions of points. While materials research is a relatively mature field, the extent to which the gathered data is publicly available is quite small, comparatively [23]. As such, this project aims to use machine learning approaches, but the inherent difficulty due to relatively small dataset size presents complications.

ASCENDS

While the fundamental mathematics of machine learning are well established, the implementation of that can be challenging to the non-mathematician. Advanced data SCiENce toolkit for Non-Data Scientists (ASCENDS) [24]is a toolkit that was developed to assist scientists or any persons who want to use their data for machine learning, with the explicit aim of making data science tools, including advanced regression analysis, principal component analysis,

and machine learning available through a user interface. In this study, the ASCENDS package is used to train a neural network with the aim of using it to predict the mechanical properties.

1.8. Conclusion

Chapter 1 detailed the L-PBF process and issues that can arise during it. The body of literature indicates that there are many variables that may have an impact on the mechanical properties of a part produced through L-PBF. Meaningful parameters exist at the powder, the scan strategy, and the laser settings. This work only examines the effects of laser settings (scan speed, hatch spacing, and laser power) on the mechanical properties of the as-built part. Future chapters will detail the samples used in this work, how they were manufactured, the methods used for mechanical and microstructural testing, and the results of the statistical analysis of that data.

2. Chapter 2: Sample Fabrication

Samples in this study were manufactured in a 3D Systems ProX 320 laser powder bed fusion system. This system has a build volume of 275mm x 275mm x 420mm and an Nd-YAG fiber laser with a nominal power of 500w, operating at a wavelength of 1070 nanometers.

All of the samples were built from 316L stainless steel powder (LaserForm 316L), with a D95 of 45 microns and a D5 of 15.56 microns. D95 designates the particle diameter 95% of the powder is smaller than, and the D5 is smaller than 5% of the powder. This powder was manufactured through the EIGA process and then processed to ensure that the specification for the particle size range is met.

An atmosphere of pure Argon was used in the build chamber for all builds in order to minimize impurities. The builds were conducted using a layer thickness of 60 microns. This was held constant for all samples across the three builds.

Laser power, hatch spacing, and scan speed were varied for the three builds. For Build 1, one process variable was modified at a time. Laser power, scan speed, or hatch spacing were varied up to 20% of their nominal value. In Build 2, two parameters were adjusted in combination, up to 20% each, and in Build 3, all three parameters were adjusted. The range of process parameter sets provided a set of linear energy densities ranging from 0.22 J/mm to 0.5 J/mm. In total, 116 unique parameter sets were used, and mechanical properties were evaluated using samples built with each set of parameters. These parameter sets are listed in Table 2. Parameter sets were iteratively generated in order to fully explore the three-dimensional space of possible parameters, as shown in Figure 6.

The samples were built 3mm off of the build plate and then removed from the build plate using wire electrical discharge machining (WEDM), and then processed via WEDM to the final dogbone geometry shown in Figure 7. The location of each sample on the build plate was randomized in order to minimize the effects of gas flow and recoating as sources of systemic error in this study.

Figure 8 shows the layout of samples on the build plate. One hundred twenty samples were manufactured per build. All samples were built in the X-Z plane in the form of 4mm x 10mm x 65mm “walls.” After building, the completed builds were subjected to a stress relief heat treatment in vacuum at 800F for two hours.

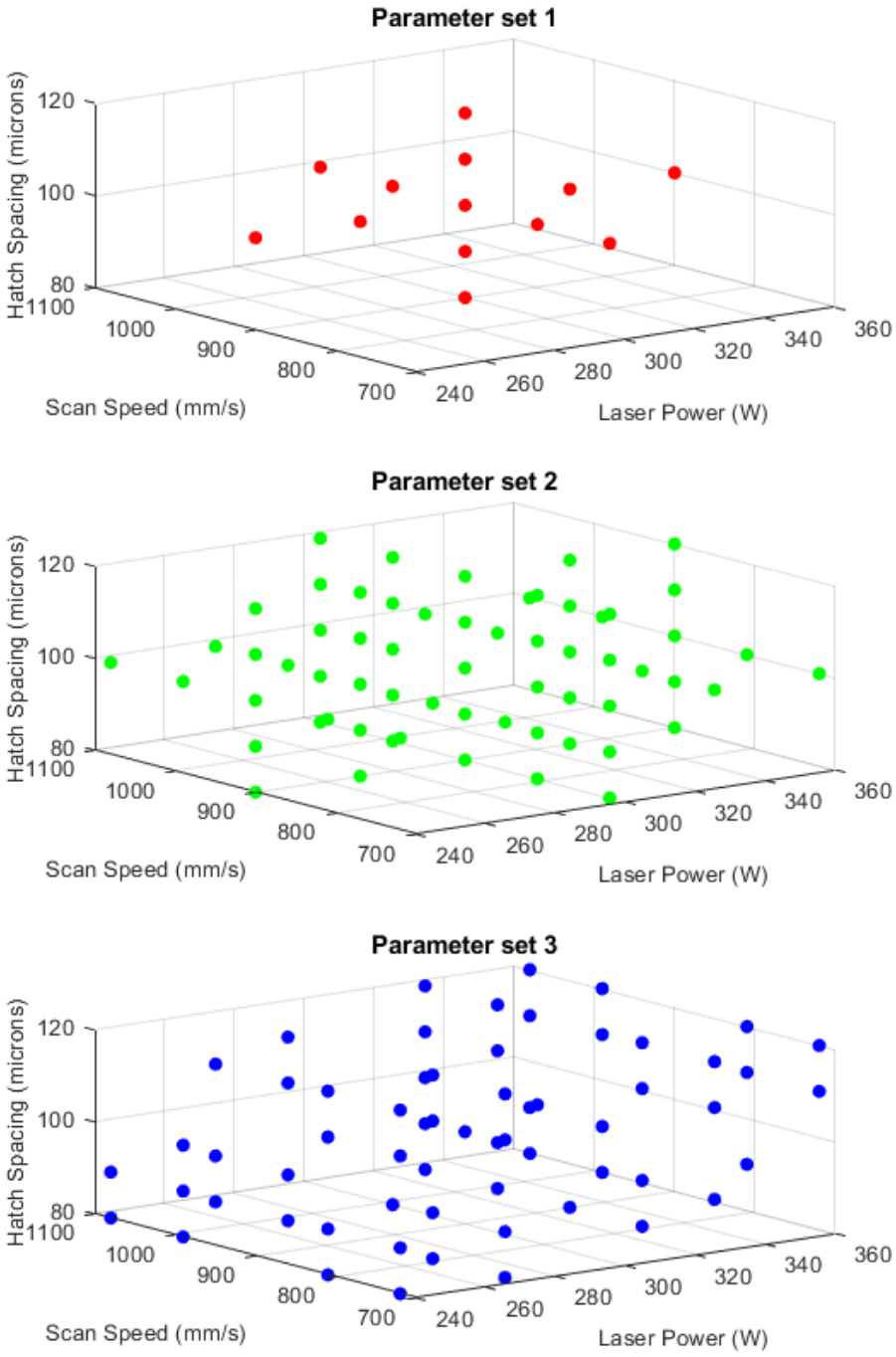

Figure 6. Visualization of laser scan parameters used in this study. The parameter space is uniformly explored in order to explore trends in the impact of process parameters on mechanical properties and microstructure. Parameter set 1 is used for build 1, parameter set 2 is used for build 2, and parameter set 3 is used for build 3.

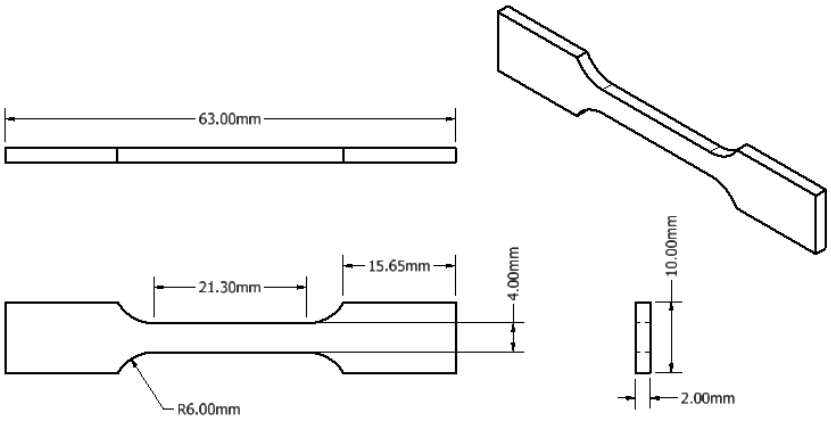

Figure 7. Dogbone tensile specimen used for uniaxial tensile testing.

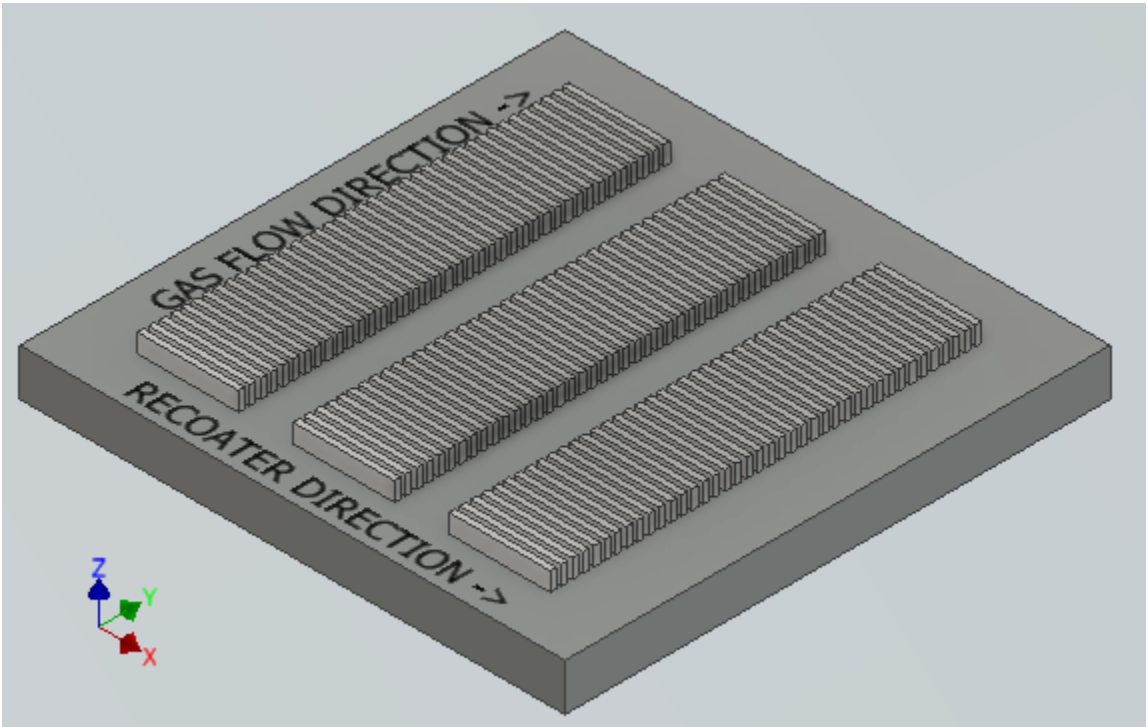

Figure 8. Layout of samples on the ProX320 build plate. The 120 walls are oriented with the short transverse in the XY plane, the long transverse in the YZ plane and the very long transverse in the XZ plane.

Table 2. List of 116 unique parameter sets used in this study.

Set #	Laser power (W)	Scan speed (mm/s)	Hatch spacing (μm)	Linear Energy Density (J/mm)
1	300	990	100	0.30
2	300	1080	100	0.28
3	300	810	100	0.37
4	300	720	100	0.42
5	300	900	100	0.33
6	330	900	100	0.37
7	360	900	100	0.40
8	270	900	100	0.30
9	240	900	100	0.27
10	300	900	110	0.33
11	300	900	120	0.33
12	300	900	90	0.33
13	300	900	80	0.33
14	330	900	120	0.37
15	300	990	80	0.30
16	300	990	110	0.30
17	300	720	80	0.42
18	330	810	100	0.41
19	300	720	120	0.42
20	300	810	80	0.37
21	330	900	80	0.37
22	300	1080	90	0.28
23	330	900	110	0.37
24	240	900	80	0.27
25	360	720	100	0.50
26	240	810	100	0.30
27	300	810	110	0.37
28	270	900	110	0.30
29	300	720	110	0.42
30	270	720	100	0.38
31	300	990	120	0.30
32	240	1080	100	0.22
33	270	810	100	0.33
34	270	900	120	0.30
35	270	900	90	0.30
36	360	900	90	0.40
37	360	900	110	0.40

Set #	Laser power (W)	Scan speed (mm/s)	Hatch spacing (μm)	Linear Energy Density (J/mm)
38	240	720	100	0.33
39	300	810	120	0.37
40	240	990	100	0.24
41	330	720	100	0.46
42	360	810	100	0.44
43	330	990	100	0.33
44	330	1080	100	0.31
45	330	900	90	0.37
46	360	900	120	0.40
47	360	900	80	0.40
48	240	900	110	0.27
49	270	900	80	0.30
50	300	1080	80	0.28
51	360	1080	100	0.33
52	300	990	90	0.30
53	360	990	100	0.36
54	240	900	120	0.27
55	240	900	90	0.27
56	300	1080	110	0.28
57	300	810	90	0.37
58	300	720	90	0.42
59	270	1080	100	0.25
60	300	1080	120	0.28
61	270	990	100	0.27
62	270	990	120	0.27
63	270	720	120	0.38
64	240	720	80	0.33
65	360	990	90	0.36
66	240	810	90	0.30
67	330	720	110	0.46
68	240	810	110	0.30
69	360	1080	110	0.33
70	240	810	80	0.30
71	330	720	120	0.46
72	330	1080	90	0.31
73	360	810	120	0.44
74	360	990	110	0.36
75	240	990	90	0.24
76	360	1080	120	0.33

Set #	Laser power (W)	Scan speed (mm/s)	Hatch spacing (μm)	Linear Energy Density (J/mm)
77	330	990	120	0.33
78	270	720	110	0.38
79	330	990	110	0.33
80	270	1080	110	0.25
81	360	810	110	0.44
82	270	810	110	0.33
83	270	990	90	0.27
84	270	810	90	0.33
85	270	720	80	0.38
86	360	990	120	0.36
87	270	810	80	0.33
88	330	810	90	0.41
89	330	1080	80	0.31
90	330	810	80	0.41
91	240	990	80	0.24
92	270	1080	80	0.25
93	240	720	120	0.33
94	330	990	80	0.33
95	240	1080	90	0.22
96	360	990	80	0.36
97	360	720	110	0.50
98	330	720	90	0.46
99	330	810	120	0.41
100	360	1080	90	0.33
101	240	1080	80	0.22
102	240	810	120	0.30
103	270	990	110	0.27
104	270	810	120	0.33
105	330	990	90	0.33
106	270	990	80	0.27
107	360	1080	80	0.33
108	270	720	90	0.38
109	330	1080	120	0.31
110	330	1080	110	0.31
111	240	720	110	0.33
112	360	720	120	0.50
113	240	720	90	0.33
114	330	810	110	0.41
115	360	810	90	0.44

Set #	Laser power (W)	Scan speed (mm/s)	Hatch spacing (μm)	Linear Energy Density (J/mm)
116	270	1080	90	0.25

2.1. Conclusion

This chapter detailed the design of the mechanical test specimens, a modified ASTM E8 uniaxial test specimen, as well as the build layout. Additionally, a list of unique processing parameters was presented, illustrating the processing parameter window used. Future chapters will detail the mechanical testing performed on the samples, as well as the procedure and results of the microstructural analysis. The results of a statistical analysis of the processing parameters and of their impact on the mechanical properties and the interaction of process-properties and structure will be discussed.

3. Chapter 3: Sample Analysis

3.1. Mechanical Testing

Strain measurements were captured by the use of digital image correlation (DIC), shown in Figure 9. Digital image correlation evaluates computational features in the image and tracks their displacement, producing a two or three-dimensional map of strain [25]. Samples are prepared for digital image correlation by the application of a "speckle pattern," which is applied using aerosolized paint. In order to improve feature tracking, a base coat of white paint is applied, and then the speckle pattern is applied, with the final speckle coating shown in Figure 9a.

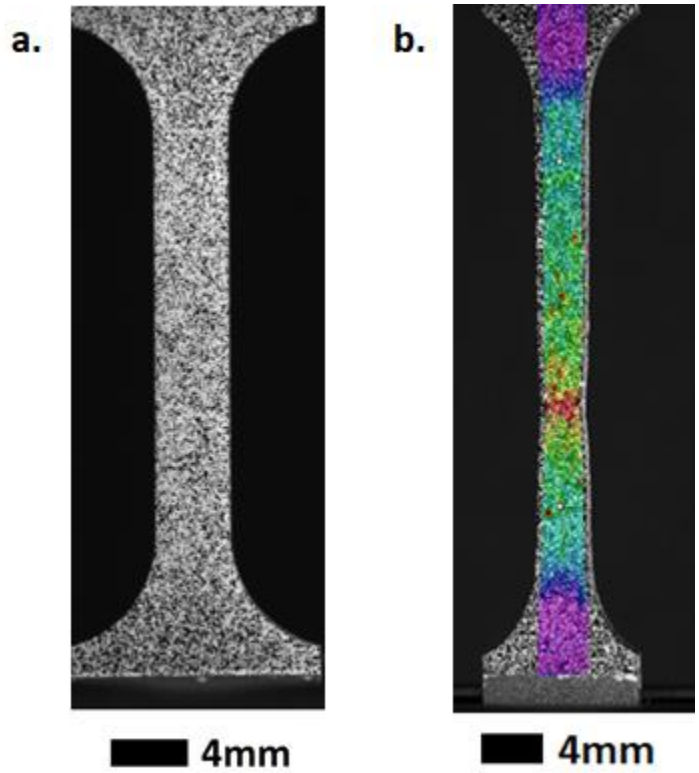

Figure 9 a) Sample with speckle pattern applied. Sample is dogbone geometry with a white base coat and black speckle pattern. b) sample with Digital Image Correlation measurements of strain as represented by the RGB color field with red indicating higher local strain values.

Mechanical testing was performed to evaluate the mechanical properties of the AM samples. Mechanical properties were measured in uniaxial tension, under quasi-static loading conditions. A strain rate of .002 s^{-1} was used on an MTS C44 dual-column load frame equipped with a 10kN load cell and manually operated specimen grips. Images for DIC were collected at a rate of 1 Hz. After the collection of data through the strain field, the images are analyzed with the digital image correlation software VicSnap 2009, by Correlated Solutions. This software tracks the changes in the captured image sequence, resulting in the calculation of a two-dimensional strain field, as shown in Figure 9b.

3.2.Microstructural analysis

It is industrially useful to be able to make an educated prediction of mechanical properties by looking at the microstructure of a material. The most widely used technique for doing this is calculating a predicted yield strength using the Hall-Petch relationship. The relation between yield stress and grain size is described mathematically by the Hall–Petch equation

$$\sigma_y = \sigma_0 + \frac{k_y}{\sqrt{d}} \qquad \text{Eq (3)}$$

Average grain diameter is traditionally evaluated using ASTM standards involving one of three methods, per ASTM E112-13:

1. *Comparison Procedure* - The comparison procedure does not require the counting of either grains, intercepts, or intersections but involves a comparison of the grain structure under examination to a series of standard images. Repeatability and reproducibility of comparison chart ratings are generally ±1 grain size number [26].
2. *Planimetric Procedure* - The planimetric procedure involves an actual count of the number of grains within a known area. A precision of ±0.25 grain size units can be attained via the planimetric method with a reasonable amount of effort [26].

3. *Intercept Procedure* - The intercept method involves an actual count of the number of grains intercepted by a test line or the number of grain boundary intersections with a test line per unit length of the test line. A precision of better than ±0.25 grain size units can be attained with a reasonable amount of effort using the intercept procedure [26].

The grain size returned by these traditional methods of grain size measurement is the Grain Size Number, defined as "the number of grains per square inch at 100X magnification" [26]. However, the traditional grain size measures are designed around columnar or equiaxed grains, which are not commonly seen in additive manufacturing. This leads to the need for more advanced methods of characterizing microstructures. Thus, a more robust technique is the use of electron backscatter diffraction (EBSD) as discussed next.

3.2.1. Electron backscatter diffraction

Electron backscatter diffraction (EBSD) analyzes the diffraction patterns that are formed from backscattered electrons that originate from an electron beam incident to the surface being analyzed. Because of Bragg's law, shown in Equation 4.:

$$n\lambda = 2dsin\theta \qquad \text{Eq (4)}$$

Electrons that are incident to the surface at an angle that satisfies the Bragg condition are diffracted in coherent patterns, known as Kikuchi patterns, shown in Figure 10. These patterns are reflected onto a phosphor screen, where a charge-coupled device camera observes them. After the images of each pattern are captured, these patterns can be analyzed with the aid of computational tools and used to calculate the orientations and phases of crystallographic regions in the material.

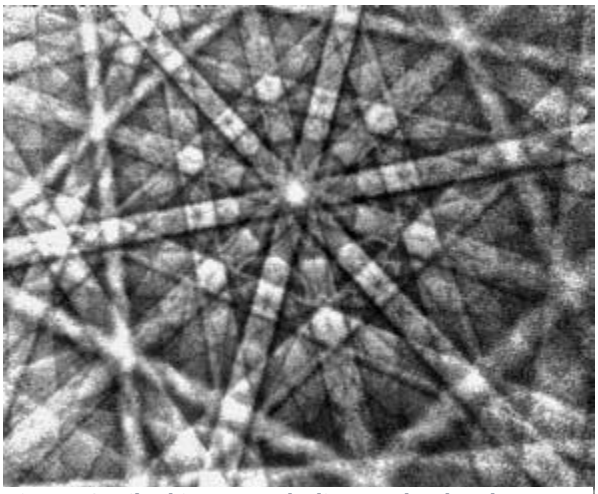

Figure 10. Kikuchi pattern. The lines on the phosphor screen are from inelastically scattered electrons that have satisfied the Bragg condition. Angles between the lines can be used to determine the crystallographic orientation of the material. [23]

Because of the sensitivity of the measurement technique, an exceptionally flat surface is needed. This makes the preparation of samples for EBSD critical. As computational techniques are used to solve the crystallographic orientation from the reading of the Kikuchi bands, a weak Kikuchi signal will result in "no solution," a result of there being no detectable Kikuchi bands visible to the detector. This "no solution" can exist as a result of surface roughness that distorts the free path of electrons as they are backscattered out of the material [27].

3.3. Sample preparation

After mechanical testing, samples were sectioned using a high-speed water-cooled cutoff saw to isolate the grip region of the dogbone tensile specimen. This sectioning was chosen to focus on examining the microstructure outside of the gauge region. In the gauge region, the sample is plastically deformed, and this distorts the microstructure. By looking at the sample in the grip region, it is possible to look at the as-built microstructures. After sectioning, samples were mounted using an Allied TechPress 3 in glass-filled mounting powder, following

recommended procedures per Allied High Tech [28]. After mounting samples, samples were polished using an Allied High Tech automatic polisher. Table 3 details the grinding steps used. Table 4 details the polishing steps used. The polishing procedure was designed to prepare samples for Electron Backscatter Diffraction (EBSD), which requires an exceptionally flat surface.

Table 3. Grinding steps used for metallographic sample preparation

Grit	Force per sample (N)	Time (min)	Platen RPM	Sample RPM	Direction of rotation
240	36	Until uniform	150	150	Contra
400	28	2’ twice	150	150	Contra
800	28	2’ twice	150	150	Contra
1200	28	2’ twice	150	150	Contra

Table 4. Polishing steps used for metallographic preparation

Grit (Micron)	Material	Time	Force per sample (N)	Platen RPM	Sample RPM	Direction of rotation
3	Polycrystalline diamond (PCD)	7’	18	250	150	Contra
1	PCD	7’	18	250	150	Contra
0.3	Al_2O_3	7’	18	150	150	Contra
0.05	Al_2O_3	7’	18	150	150	Contra

3.4.EBSD Analysis

EBSD was performed on samples from multiple different builds. Twenty-nine samples in total were analyzed using EBSD. Table 5 shows the nominal scan parameters used for the EBSD analysis. The EBDS analysis was performed over a number of sessions, and care had to be taken to replicate the imaging conditions in order to ensure consistently high-quality data. Figure 11 shows a representative scan from a 316L sample, with grains colored.

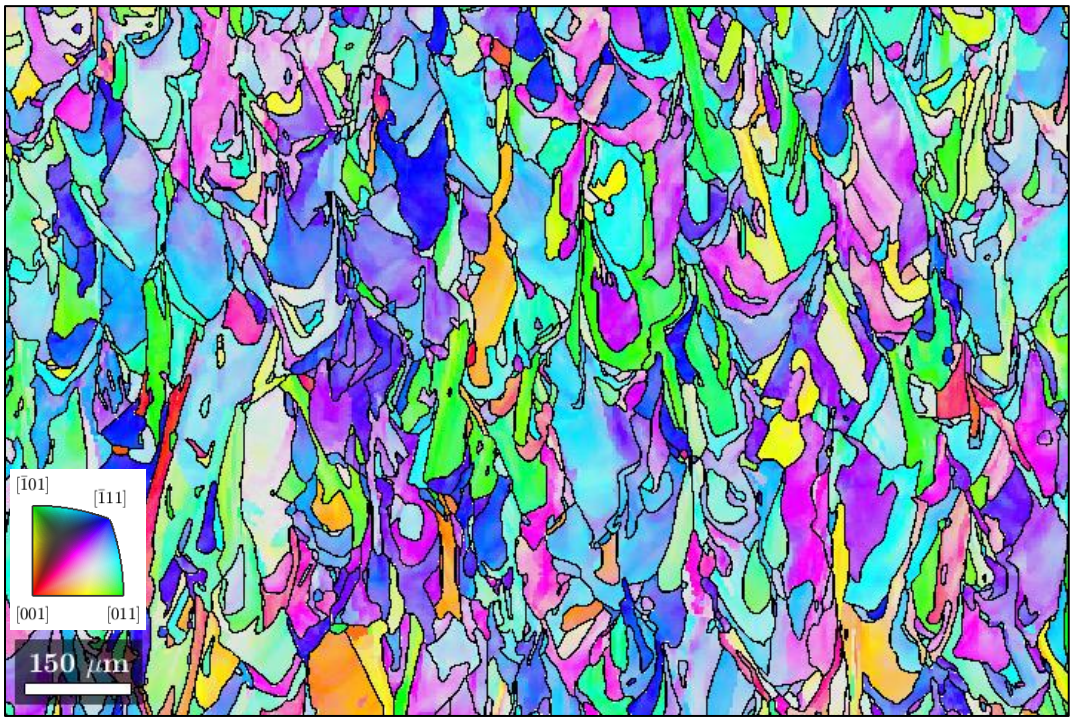

Figure 11. Results from the EBSD analysis of 316L.Build direction is upward on the page. The legend on the right communicates the relationship between grain orientation and color.

After the scan of the EBSD data was performed, it is necessary to process the data in order to extract meaningful features. This is performed using MTEX, a free MATLAB toolbox for analyzing and modeling crystallographic textures by means of EBSD or pole figure data. This software reads the crystallographic mapping from the EBSD analysis and performed cleaning and filtering operations, allowing the data to be used for statistical representation.

Table 5. EBSD and associated SEM microscope scan parameters.

Acceleration (kV)	25
Filament Current (nA)	13
Specimen tilt (deg)	70
Binning	6x6
Gain	1
Exposure Time (ms)	Automatic
Spot Size (um)	3
Scan area (mm^2)	1.5
Grain Mapping	
Critical Misorientation	10
Boundary completion (degrees)	1
Minimum grain area (pixels)	10

3.5.Etching

After the samples are measured using EBSD, they are etched to reveal microstructural features for optical microscopy. While EBSD will report crystallographic information, it will not produce information on features that exist outside of or within grains, for example, weld pools or cells. In this work, the etching procedure used is an electrochemical etch in oxalic acid. The oxalic acid is maintained at a temperature sufficient to keep the oxalic acid in solution. The mounted samples are immersed in the oxalic acid solution, and then a current is applied via a conventional probe. The voltage used is governed by a regulated power supply, set to provide 3 volts. This current is applied using a sharp probe, and applied for a short period, approximately 2 seconds, depending on expert judgment. After the etching is complete, many more microstructural features are visible.

3.5.1. Cell size analysis

The grains contain sub-granular solidification features referred to as cells. It is widely understood that there is a link between process parameters and cell sizes with a higher cooling rate generating finer cellular structures, as shown in Figure 12 [1], [29]. While it is widely understood that the processing parameters impact the size of the cellular structure, the relationship between cell size and mechanical properties is less well understood [29], [30].

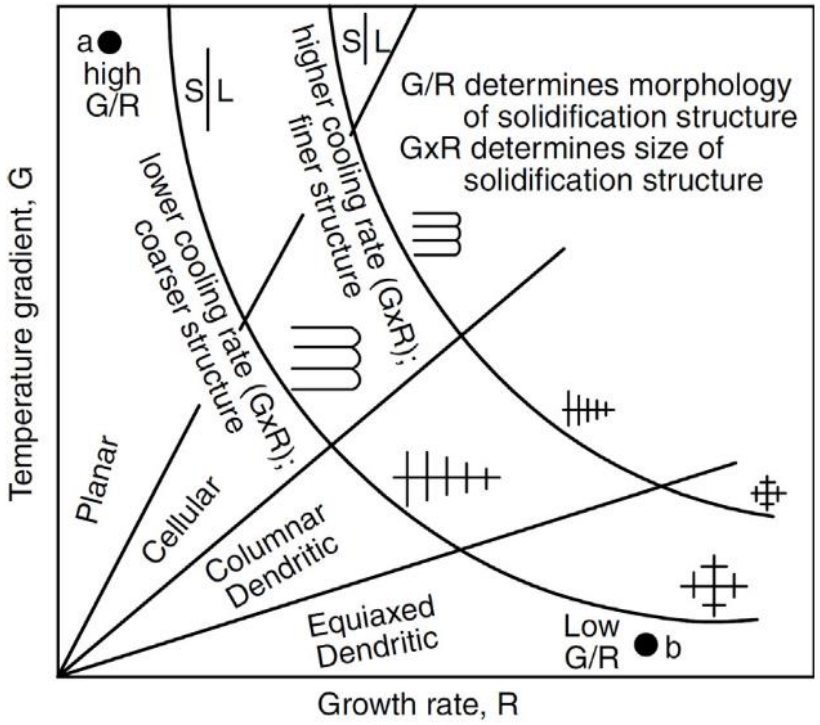

Figure 12. G/R plot demonstrating the impacts of temperature gradient G and growth rate R on the morphology solidification structures [1].

In this work, the cell sizes are measured from micrographs collected by Scanning Electron Microscope, with Fiji [31], a standard open-source image analysis software package. For each collected SEM image, a representative sample of cells is measured, approximately 50-70 measurements, with 2-3 images per sample collected. This is used as the defined cell size for the set of process parameters. A solidification cell will be bisected during the metallographic

preparation process and visible as an ellipse under electron microscopy. To compensate for geometric distortion, cell measurements are taken as the minor diameter of the cell.

3.6. Conclusion

This chapter detailed the test methods used for mechanical as well as microstructural analysis. Samples in this study were tested in uniaxial tension at a quasi-static straing rate. Strain was captured using digital image correlation. After mechanical test, the samples were prepared for metallography. Microstructural data was collected using electron backscatter diffraction (EBSD). After microstructural data was collected, the samples were etched and solidification cells were imaged using scanning electron microscopy Future chapters will detail the results of the mechanical testing and the microstructural analysis. A statistical analysis will be performed to determine links between processing parameters and mechanical and microstructural properties.

4. Chapter 4: Results and Conclusion

4.1. Mechanical analysis

In order to derive relationships between processing parameters and mechanical properties, a series of statistical analyses are done. Minitab® 17 Statistical Software is used for the purpose of analyzing this data. Mechanical property measurements and corresponding process parameter values were imported into Minitab, and the dataset was evaluated to detect and remove outliers. The method used to determine outliers was a value outside of 3 standard deviations from the mean. The mean yield strength is 569.469 MPa, with a standard deviation of 10.28 MPa. This resulted in the removal of two data points, one a high outlier and one a low outlier. Additionally, data points collected with errors in the testing, such as premature breakage (sample breaking at <20% strain) or sample slipping in the grip, were excluded. After this, a total of 339 samples were collected for analysis.

After removing the two outliers, the data was tested for normality by the Anderson-Darling normality criteria [32]. Under this criterion, the test for normality returns a P-value of 0.445, greater than the test criteria of 0.05, giving us valid evidence that the sample fits a normal distribution. This allows us to work directly with the data and not apply any transformations to achieve normality. It was found that the yield strength data possesses a skewness of -0.088 and a kurtosis of -0.37, reinforcing the fact that the data fits a normal distribution.

With these samples, a two-sided t-test was performed on the collected data, grouped by volumetric energy density (VED). The mean value at each VED (for VEDs with greater than one sample) for engineering yield strength (EYS) maximum elongation (ME), and ultimate tensile strength (UTS) was compared to the overall mean and tested for statistical significance. Contrary

to what we expect, we see statistically significant mean differences across the entire range of volumetric energy densities. The results of this series of analyses are shown in Table 6. This suggests that an analysis of variation that takes into account interactions between processing parameters would be a useful step.

Table 6. Two-sided t-tests for samples manufactured at every volumetric energy density with more than one sample. Statistically significant differences are found across the range of volumetric energy densities.

VED	**EYS**	**ME**	**UTS**
37.04	yes	no	yes
37.88	yes	yes	yes
40.4	no	yes	yes
41.15	yes	no	yes
41.32	yes	yes	yes
41.67	no	no	no
42.09	no	no	no
44.44	no	yes	yes
44.89	no	no	yes
45.91	yes	yes	no
46.3	no	no	yes
49.38	yes	no	no
50	no	no	yes
50.51	no	no	yes
50.93	yes	no	no
51.44	yes	no	no
52.08	no	no	no
54.87	yes	yes	yes
55.56	yes	no	no
56.12	no	yes	no
56.58	no	no	no
56.82	no	no	no
57.87	yes	no	no
60.61	yes	no	yes
61.11	no	no	no
61.73	no	no	yes
62.5	no	no	yes
63.13	no	no	yes
63.66	no	no	no

VED	EYS	ME	UTS
66.67	no	yes	yes
67.34	yes	no	no
67.9	yes	no	yes
69.44	yes	no	yes
74.07	no	no	yes
75.45	no	yes	yes
75.76	no	yes	no
76.39	yes	no	yes
83.33	yes	yes	yes
84.88	no	yes	yes

Table 7. Results of all analyses of means. It was found that at no point does the modification of scan parameters result in a sample mean that escapes the decision surface.

	Scan Speed	Laser Power	Hatch Spacing
EYS	No	No	No
UTS	No	No	No
EPS	No	No	No
SF	No	No	No

After testing the data for normality, an analysis of means (ANOM) was performed on each of the three scan parameters (laser power, scan speed, and hatch spacing) and was used to look for an effect on the mean engineering yield strength (EYS) of each treatment group (the collection of all yield strengths at a particular laser power, scan speed or hatch spacing). Representative results from the ANOM study between EYS and laser power are shown in Figure 13. Based on this analysis, we cannot say that laser power has a significant effect on the mean yield strength of the sample. However, in evaluating this data, we are varying multiple factors at a time and must expand our analysis to account for that.

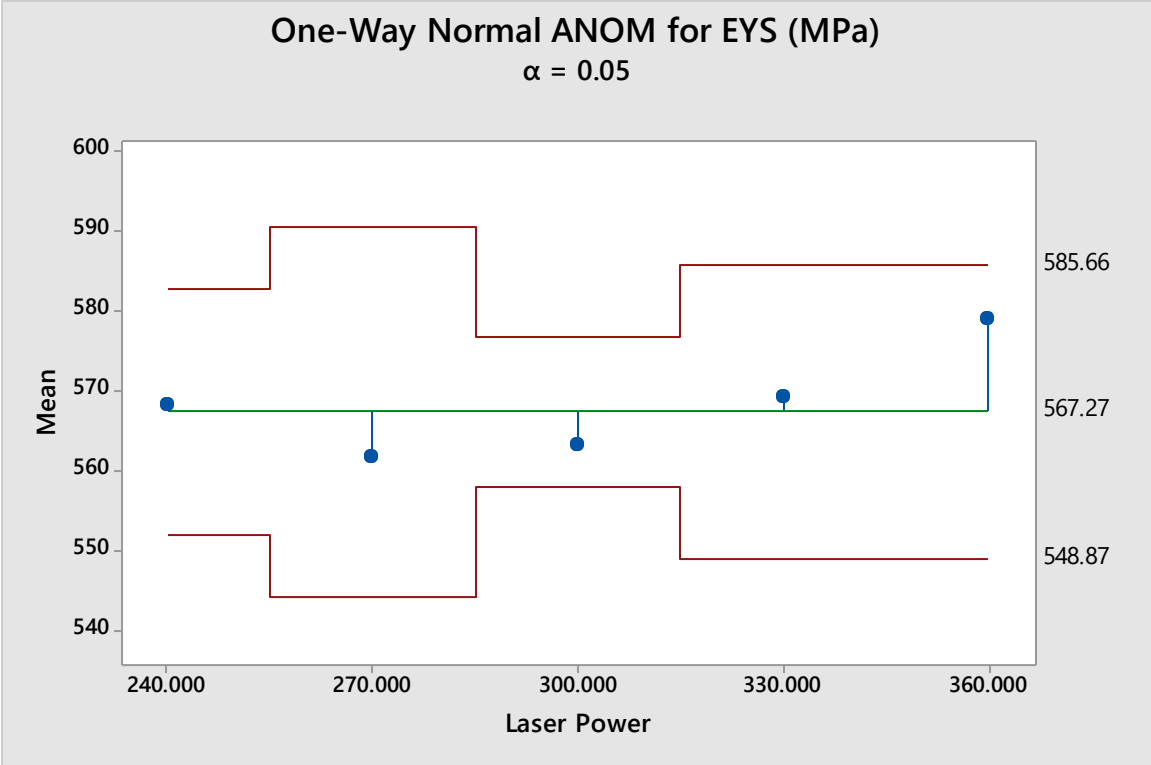

Figure 13. Analysis of means between treatment groups in this study. We see no significant response (outside of the red decision line) at any treatment level.

An analysis of variation (ANOVA) was performed on the data in order to examine the effects of the three process parameters on three mechanical properties. The ANOVA was

performed to a confidence interval of 95% with a critical p-value of 0.05. The results of these analyses are shown in Table 8, Table 9, and Table 10.

The ANOVA in Table 8 is evaluating the effects of our processing parameters on engineering yield strength. In this analysis, we see that there are P-Values lower than our critical value for laser power, hatch spacing, and the interaction of laser power and hatch spacing. For these factors, we assume that a variation will have a statistically significant effect on the engineering yield strength. In the applicability of this model, we see a p-value for "lack of fit error" of 0.01, indicating that the model is not able to represent our data in a statistically significant way. Table 9 is evaluating the effects of our processing parameters on strain at failure. In this analysis, we see that there are p-values lower than our critical value for all of our test parameters except for laser power * scan speed and scan speed * hatch spacing. In the applicability of this model, we see a p-value for "lack of fit error" of 0.02, indicating that the model is not able to represent our data in a statistically significant way.

Table 8. ANOVA for the effects of laser power, scan speed and hatch spacing on engineering yield strength

Analysis of Variance

Source	DF	Seq SS	Contribution	Adj SS	Adj MS	F-Value
Laser power (W)	4	2671.9	6.78%	1341.0	335.25	3.51
Scan speed (mm/s)	4	451.0	1.14%	804.0	200.99	2.10
Hatch spacing (um)	4	3413.2	8.66%	2381.1	595.27	6.23
Laser power (W)*Scan speed (mm/s)	16	890.9	2.26%	639.2	39.95	0.42
Laser power (W)*Hatch spacing (um)	16	2939.7	7.46%	2904.5	181.53	1.90
Scan speed (mm/s)*Hatch spacing (um)	16	2480.8	6.29%	2480.8	155.05	1.62
Error	278	26582.8	67.42%	26582.8	95.62	
Lack-of-Fit	53	7823.2	19.84%	7823.2	147.61	1.77
Pure Error	225	18759.5	47.58%	18759.5	83.38	
Total	338	39430.4	100.00%			

Source	P-Value
Laser power (W)	0.008
Scan speed (mm/s)	0.081
Hatch spacing (um)	0.000
Laser power (W)*Scan speed (mm/s)	0.977
Laser power (W)*Hatch spacing (um)	0.021
Scan speed (mm/s)*Hatch spacing (um)	0.063
Error	
Lack-of-Fit	0.002
Pure Error	
Total	

Table 9. ANOVA for the effects of laser power, scan speed, and hatch spacing on strain at failure.

Analysis of Variance

Source	DF	Seq SS	Contribution	Adj SS	Adj MS
Laser power (W)	4	0.02640	5.08%	0.026157	0.006539
Scan speed (mm/s)	4	0.01958	3.77%	0.007904	0.001976
Hatch spacing (um)	4	0.09946	19.15%	0.066293	0.016573
Laser power (W)*Scan speed (mm/s)	16	0.02264	4.36%	0.041384	0.002586
Laser power (W)*Hatch spacing (um)	16	0.05125	9.87%	0.067359	0.004210
Scan speed (mm/s)*Hatch spacing (um)	16	0.05131	9.88%	0.051310	0.003207
Error	278	0.24883	47.90%	0.248829	0.000895
Lack-of-Fit	53	0.06157	11.85%	0.061573	0.001162
Pure Error	225	0.18726	36.05%	0.187256	0.000832
Total	338	0.51948	100.00%		

Source	F-Value	P-Value
Laser power (W)	7.31	0.000
Scan speed (mm/s)	2.21	0.068
Hatch spacing (um)	18.52	0.000
Laser power (W)*Scan speed (mm/s)	2.89	0.000
Laser power (W)*Hatch spacing (um)	4.70	0.000
Scan speed (mm/s)*Hatch spacing (um)	3.58	0.000
Error		
Lack-of-Fit	1.40	0.051
Pure Error		
Total		

Table 10. ANOVA for the effects of laser power, scan speed and hatch spacing on ultimate tensile strength

Analysis of Variance

Source	DF	Seq SS	Contribution	Adj SS	Adj MS	F-Value
Laser power (W)	4	7462.0	13.57%	8791.8	2197.95	50.22
Scan speed (mm/s)	4	2845.1	5.17%	4661.0	1165.26	26.62
Hatch spacing (um)	4	29197.7	53.10%	19005.5	4751.38	108.56
Laser power (W)*Scan speed (mm/s)	16	1131.5	2.06%	960.6	60.04	1.37
Laser power (W)*Hatch spacing (um)	16	1348.1	2.45%	1488.0	93.00	2.12
Scan speed (mm/s)*Hatch spacing (um)	16	837.3	1.52%	837.3	52.33	1.20
Error	278	12167.2	22.13%	12167.2	43.77	
Lack-of-Fit	53	3638.4	6.62%	3638.4	68.65	1.81
Pure Error	225	8528.8	15.51%	8528.8	37.91	
Total	338	54988.9	100.00%			

Source	P-Value
Laser power (W)	0.000
Scan speed (mm/s)	0.000
Hatch spacing (um)	0.000
Laser power (W)*Scan speed (mm/s)	0.155
Laser power (W)*Hatch spacing (um)	0.008
Scan speed (mm/s)*Hatch spacing (um)	0.271
Error	
Lack-of-Fit	0.002
Pure Error	
Total	

From these analyses of variation, we can see that the different scan parameters impact each other and the mechanical properties in different ways depending on the target mechanical property. This is important to note in the design of processing conditions, as tradeoffs to achieve different mechanical properties must be made, as there are no scan parameters that only impact one mechanical property. This is evident in Figure 14, where we see graphical evidence of the

interactions between the processing parameters and the impact that has on engineering yield strength.

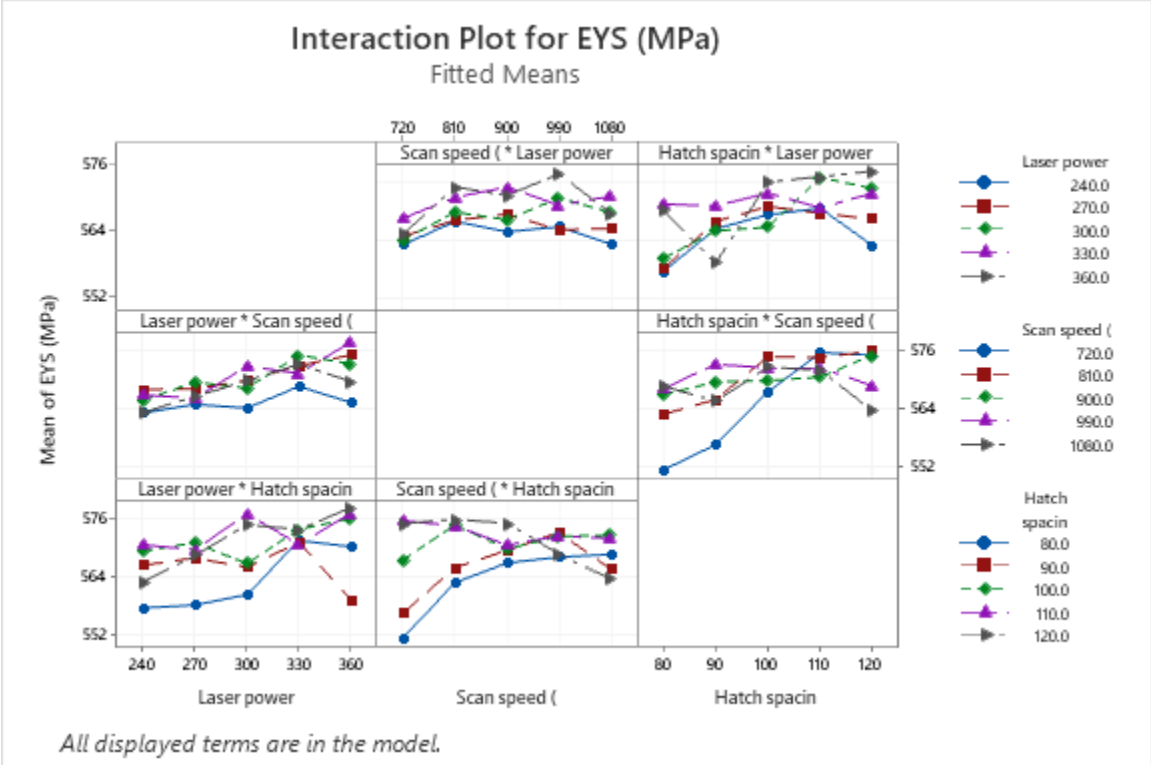

Figure 14. Interaction plots for scan speed, laser power, and hatch spacing and their effects on engineering yield strength.

4.2.Machine learning

With the results from the statistical analysis in mind, it was endeavored to attempt to develop a machine learning framework in order to predict mechanical properties with respect to processing parameters. In order to develop a predictive model for mechanical properties with respect to processing parameters, the Advanced data SCiENce toolkit for Non-Data Scientists (ASCENDS) is used to [24] generate and train a Neural Network (NN). The NN was trained on the dataset without the outliers and evaluated with laser power, scan speed, hatch spacing, as well as all combinations of the processing parameters. The model hyperparameters were dynamically tuned by ASCENDS.

Figure 15 shows the results of using the trained neural networks to predict the variables. This shows the mean absolute errors (MAE) for the results of the predictions. Lower values are better. As is shown, the selection of additional processing parameters to train the neural network is of limited benefit.

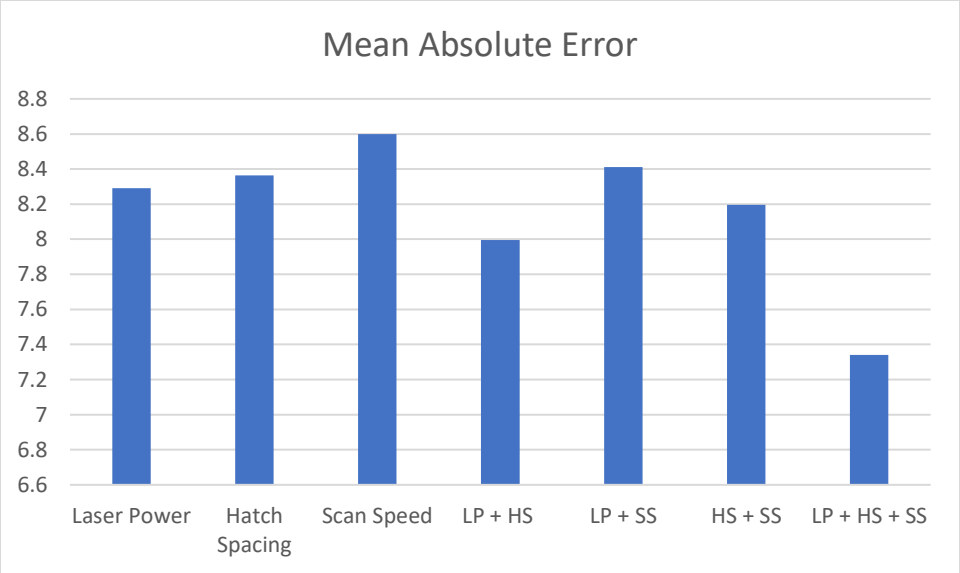

Figure 15. Mean absolute errors for neural networks trained with the listed processing parameters and combinations thereof.

4.3.Microstructural analysis

4.3.1. EBSD Analysis

A subset of 20 samples, listed in Table 11, across all three builds, were analyzed using Electron Backscatter Diffraction (EBSD). These samples were analyzed for grain misorientation and gran sizes and analyzed to identify links between processing parameters and these measurements. As an initial analysis, the data was plotted for the purposes of preliminary statistical exploration; this was followed by statistical analysis in Minitab.

Table 11. Samples from builds 1 2 and 3 that were analyzed for microstructure. Listed are process parameters, as well as linear and volumetric energy densities.

Sample	Laser power (W)	Scan speed (mm/s)	Hatch spacing (um)	Linear energy density (J/mm)	Volumetric Energy Density (J mm^{-3})
20X2	300	900	120	0.33	46.30
31x1	240	900	100	0.27	44.44
32x2	300	900	110	0.33	50.51
35x2	300	900	80	0.33	69.44
37x2	300	1080	100	0.28	46.30
39x2	300	720	100	0.42	69.44
B2S103	300	720	80	0.42	86.81
B2S105	330	810	100	0.41	67.90
B2S118	360	720	100	0.50	83.33
B2S120	270	900	110	0.30	45.45
B2S20	240	1080	100	0.22	37.04
B2S3	360	900	90	0.40	74.07
B2S51	240	900	110	0.27	40.40
B2S69	300	1080	110	0.28	42.09
B3S101	240	720	80	0.33	69.44
B3S26	330	810	80	0.41	84.88
B3S32	360	720	110	0.50	75.76
B3S58	330	1080	120	0.31	42.44
B3S79	270	1080	110	0.25	37.88
B3S98	300	900	100	0.33	55.56

Grain misorientation was analyzed as a function of volumetric energy density. MTEX was used to calculate the mean misorientation between grains, at grain boundaries, and an average misorientation along every grain boundary was calculated. The results are displayed in Figure 16. It was found that the grain misorientation precipitously declines as a function of volumetric energy density input, which is in agreement with trends reported by Ramirez-Cedillo et al. [33]. Mechanistically, we expect to see lower grain misorientations as volumetric energy density increases, as a result of more significant time to solidification in the melt, allowing for more epitaxial growth.

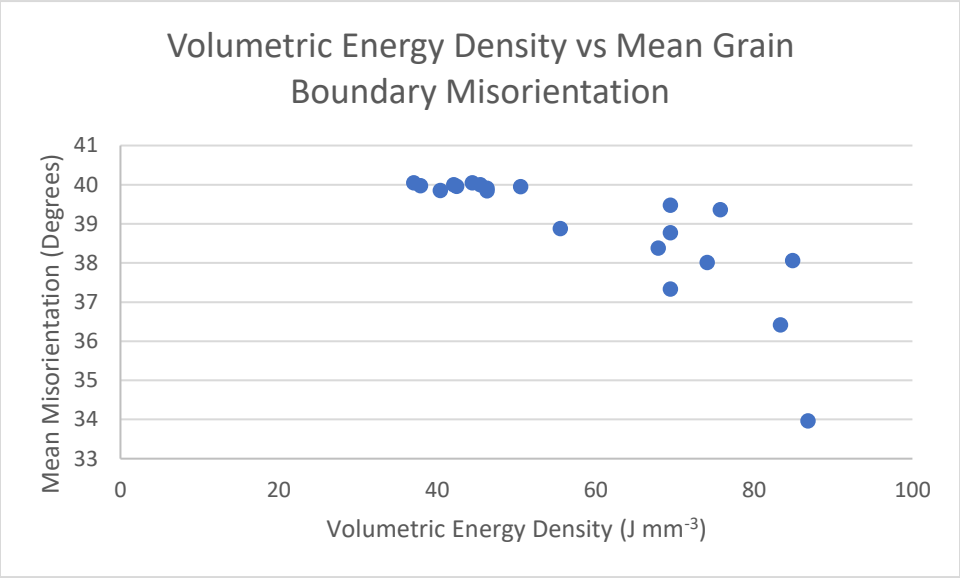

Figure 16. Volumetric Energy Density vs Mean Grain Boundary misorientation. This indicates that the misorientation between grains at the grain boundary decreases with increasing volumetric energy density.

The grain size was plotted as a function of volumetric energy density. Results from this analysis are shown in Figure 17. These results are expected based on Rosenthal simulations of grain growth. Higher volumetric energy densities create slower cooling rates, resulting in larger grains. The effect of energy density, linear or volumetric, is widely reported in the literature [13],

[12], [30], [29], but the results from this work, in addition to other published work suggest that microstructural features other than grain size influence yield and ultimate tensile strengths [29].

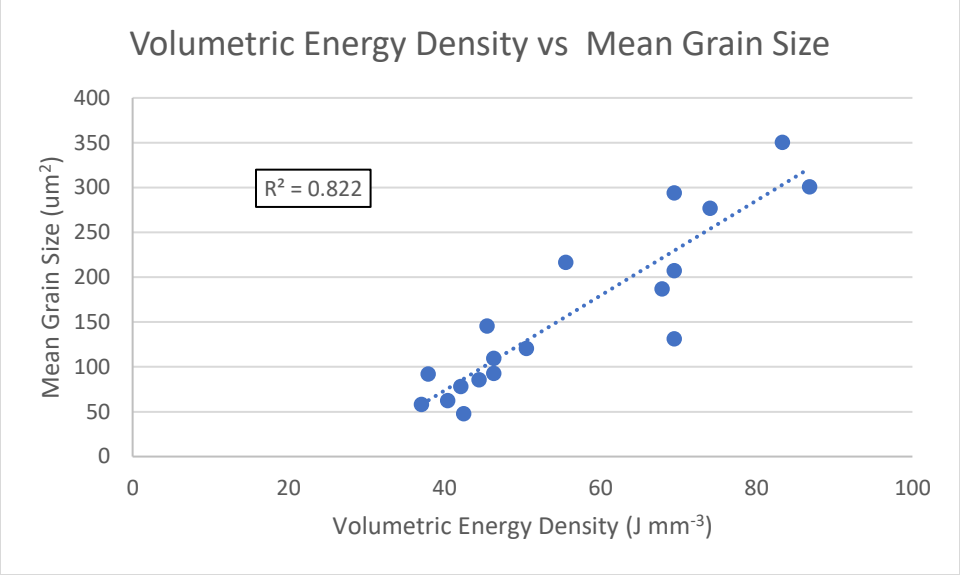

Figure 17. Volumetric Energy Density vs Mean Grain Size.

After this analysis, Minitab was used to fit a Hall-Petch equation to the grain size data, the results of which are shown in Figure 18. From the fitting of the microstructural data, the σ_0

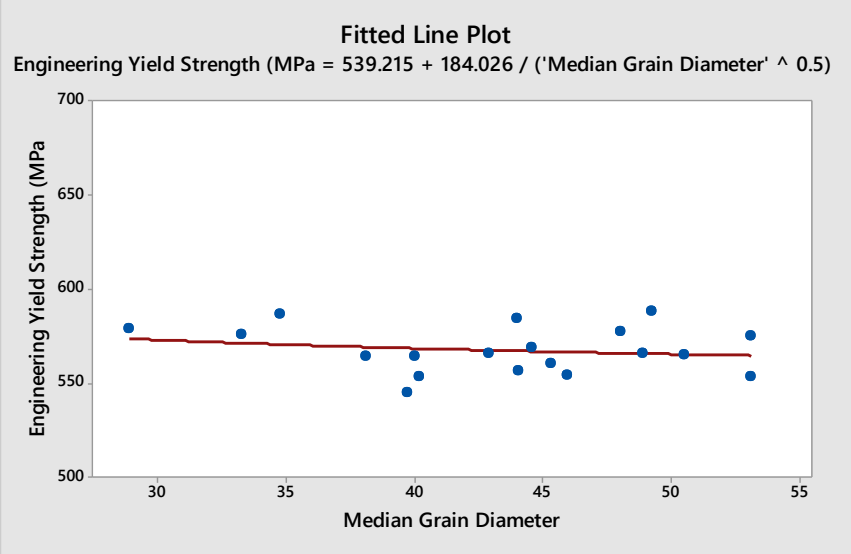

Figure 18. Results from fitting Hall-Petch curve to data collected from 316L microstructures.

value is 539.215, and the k value is 184.026. This derived Hall-Petch equation has a standard error of 12.33.

An analysis of means was performed, similar to that shown in Figure 13, in order to ascertain the effects of the processing parameters on various microstructural features. The results of these analyses are shown in Table 12. In no analysis was the calculated mean outside of the decision limit range, indicating a lack of statistically significant influence on the measured property (grain size, cell diameter, or grain boundary misorientations).

Table 12. Results from analyses of means, the impact of three processing parameters on various microstructural characteristics. "No" indicates the decision boundary was never crossed, casting doubt on a statistically significant relationship.

	Mean Grain Size	Mean Misorientation
Laser Power	No	No
Scan Speed	No	No
Hatch Spacing	No	No

4.3.2.

Cell size analysis

The samples that were analyzed with EBSD were then etched and imaged to capture the dimensions of the sub-granular solidification cells. A set of analyses of means was performed in

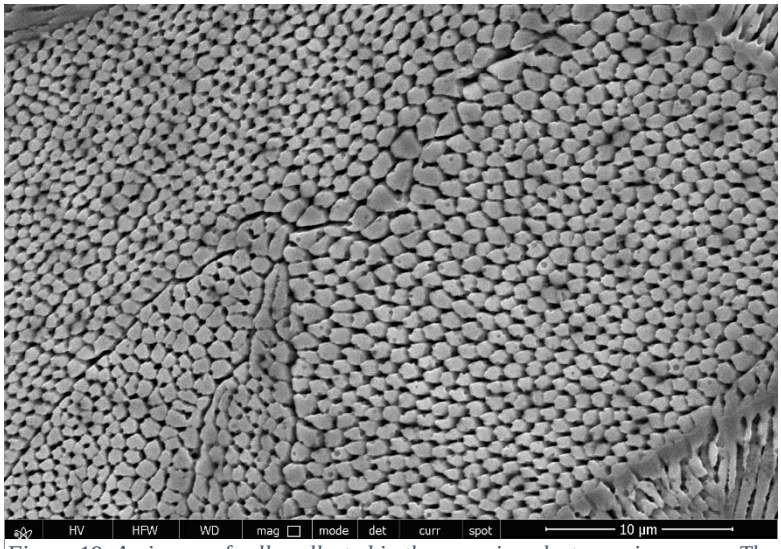

Figure 19. An image of cells collected in the scanning electron microscope. The cells collected vary in size, but are on the 0.5-1um length scale.

order to examine the effects of various processing parameters on the solidification cell size, an example of which is shown in Figure 19. The length scale of the solidification cells is generally 0.5μm to 1μm and can vary substantially within a sample based on location within a melt pool.

The collected data was fitted to a power function, in order to generate σ_0 and k constants, similar to that of a Hall-Petch equation. The results of that fitting are shown in Figure 20. Unusually, this shows an increase in engineering yield strength as mean cell diameter increases, when a typical Hall-Petch relationship between grain size and yield strength shows a decrease in yield strength as grain size increases. It is unclear what mechanism would lead to higher yield strengths with larger solidification cells. However, the correlation between mean grain diameter and the calculated power function is weak at best, and future work should clarify this.

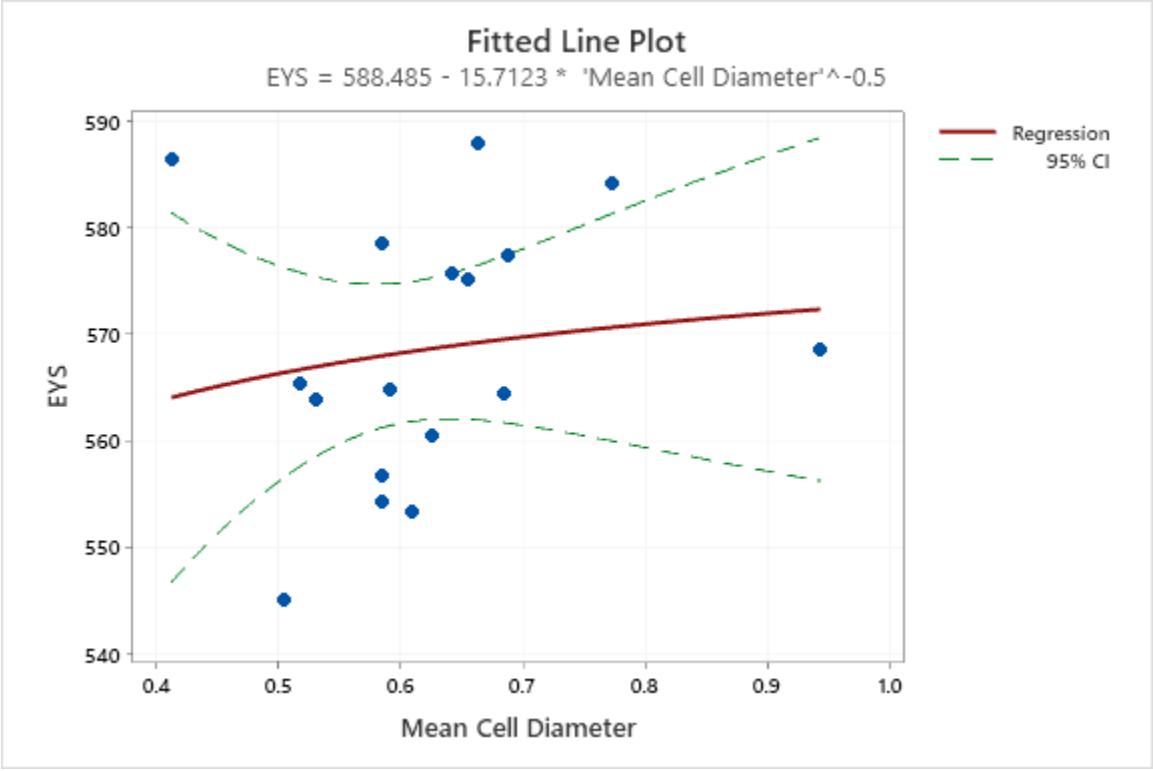

Figure 20. Results of fitting of a power function to measured cell diameter data.

An analysis of variation (ANOVA) was performed in order to ascertain the effects of interactions between parameters on the mean solidification cell size. The ANOVA was performed to a 95% confidence interval, and an interaction plot was generated and is shown in Figure 21. Based on the plotted lines in the interaction chart crossing, we infer that there is no combination of changes in processing parameters that generate a statistically significant response in the mean cell size. This result is consistent with that reported by Bertoli et al.[18], that within a relatively wide range of processing parameters, the resulting solidification structure forms a stable range of cell sizes [19].

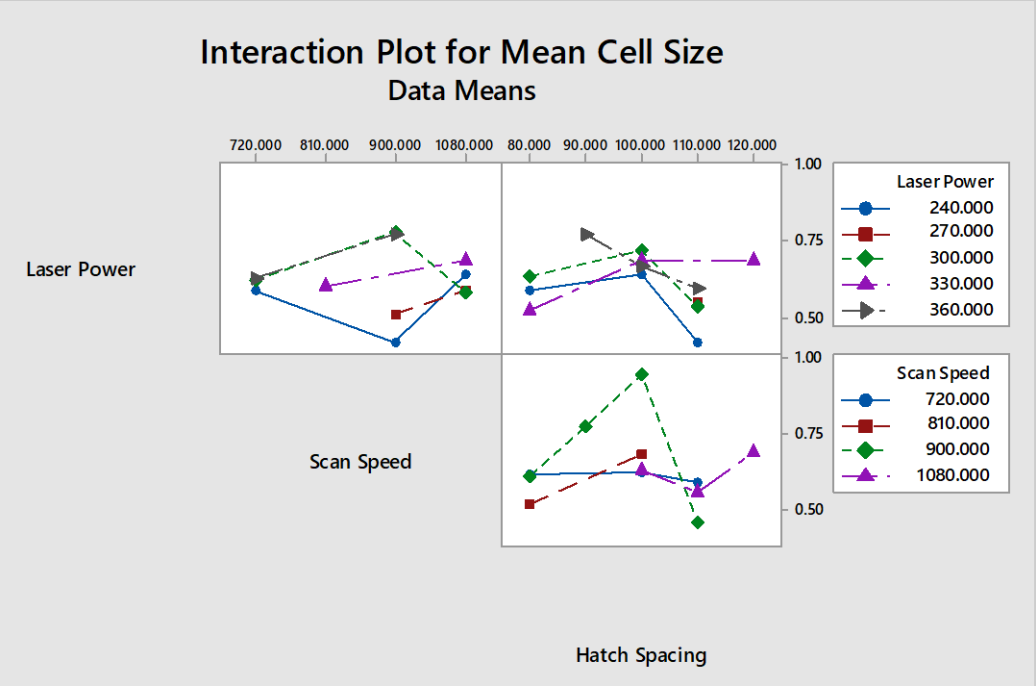

Figure 21. Interaction plot for the scan parameters on mean cell size. As the interaction plot lines intersect, we can see that there is some interaction between process parameters affecting mean cell size.

4.4. Conclusion

In conclusion, this study examining the effects of laser processing parameters on the mechanical properties and the microstructure of 316L. Three hundred and sixty samples were

manufactured in three builds, and then all were mechanically tested in uniaxial tension. After the mechanical testing, a subset of samples was used in a study of the microstructure in order to attempt to generate links between processing parameters and various microstructural features.

The following conclusions were reached:

1. Additive manufacturing has the ability to manufacture shapes with a wide range of flexibility, but the mechanical properties for parts made from AM 316L may vary within a relatively wide range
2. Mechanical properties of additively manufactured 316L vary based on processing parameters in a statistically significant way.
3. However, the range of properties examined exhibited significant variation. As a result of this variation, an attempt to train a machine learning model was met with limited success.
4. The microstructure of AM 316L appears to vary in response to process parameters, but this was unable to be used to generate a statistically significant link between processing parameters and microstructural features.

4.5.Limitations

This work aimed to expore the links between processing parameters, microstructure and mechanical properties using machine learning technologies. However, it was revealed that machine learning techniques require a great deal more data than was presented in this study.

Additionally, the study design was made unbalanced by virtue of some points in the parameter space being repeated. A balanced dataset and would allow for a more rigorous design of experiment.

4.6.Future work

Future work could be done using the techniques detailed in this paper. 316L is a dutile alloy, and its mechanical properties do not vary greatly in response to laser processing parameters. Appplying the techniques in this paper to a more brittle alloy, such as Ti64, could yield more insight into the links between processing parameters and properties.

Additionally, the number of samples used for microstructural analysis could be greatly expanded. In this work, 20 samples out of 360 were analyzed for microstructure, offering a suggestion that in the future far more samples could be submitted for analsysi, improving the analysis of links between processing parameters, mechanical properties, and, microstructure.

References

[1] T. DebRoy *et al.*, "Additive manufacturing of metallic components – Process, structure and properties," *Prog. Mater. Sci.*, vol. 92, pp. 112–224, 2018.

[2] L. E. Criales, Y. M. Arısoy, and T. Özel, "Sensitivity analysis of material and process parameters in finite element modeling of selective laser melting of Inconel 625," *Int. J. Adv. Manuf. Technol.*, vol. 86, no. 9–12, pp. 2653–2666, 2016.

[3] M. Bayat *et al.*, "Keyhole-induced porosities in Laser-based Powder Bed Fusion (L-PBF) of Ti6Al4V: High-fidelity modelling and experimental validation," *Addit. Manuf.*, vol. 30, p. 100835, 2019.

[4] H. Gong, K. Rafi, H. Gu, T. Starr, and B. Stucker, "Analysis of defect generation in Ti–6Al–4V parts made using powder bed fusion additive manufacturing processes," *Addit. Manuf.*, vol. 1–4, pp. 87–98, 2014.

[5] E. Bassoli, A. Sola, M. Celesti, S. Calcagnile, and C. Cavallini, "Development of laser-based powder bed fusion process parameters and scanning strategy for new metal alloy grades: A holistic method formulation," *Materials (Basel).*, vol. 11, no. 12, 2018.

[6] "Machinability of metals," *Engineering Toolbox*, 2020. .

[7] R. Casati, J. Lemke, and M. Vedani, "Microstructure and Fracture Behavior of 316L Austenitic Stainless Steel Produced by Selective Laser Melting," *J. Mater. Sci. Technol.*, vol. 32, no. 8, pp. 738–744, 2016.

[8] R. Saluja, "the Emphasis of Phase Transformations and Alloying Constituents on Hot Cracking Susceptibility of Type 304L and 316L Stainless Steel Welds," *Int. J. Eng. Sci. Technol.*, vol. 4, no. 5, pp. 2206–2216, 2012.

[9] P. Mercelis and J. P. Kruth, "Residual stresses in selective laser sintering and selective laser melting," *Rapid Prototyp. J.*, vol. 12, no. 5, pp. 254–265, 2006.

[10] G. Chen, S. Y. Zhao, P. Tan, J. Wang, C. S. Xiang, and H. P. Tang, "A comparative study of Ti-6Al-4V powders for additive manufacturing by gas atomization, plasma rotating electrode process and plasma atomization," *Powder Technol.*, vol. 333, pp. 38–46, 2018.

[11] P. A. Hooper, "Melt pool temperature and cooling rates in laser powder bed fusion," *Addit. Manuf.*, vol. 22, pp. 548–559, 2018.

[12] Y. M. Arısoy, L. E. Criales, T. Özel, B. Lane, S. Moylan, and A. Donmez, "Influence of scan strategy and process parameters on microstructure and its optimization in additively manufactured nickel alloy 625 via laser powder bed fusion," *Int. J. Adv. Manuf. Technol.*, vol. 90, no. 5–8, pp. 1393–1417, 2017.

[13] H. Choo *et al.*, "Effect of laser power on defect, texture, and microstructure of a laser powder bed fusion processed 316L stainless steel," *Mater. Des.*, vol. 164, p. 107534, Feb. 2019.

[14] H. Irrinki *et al.*, "Effects of Powder Attributes and Laser Powder Bed Fusion (L-PBF)

Process Conditions on the Densification and Mechanical Properties of 17-4 PH Stainless Steel," *Jom*, vol. 68, no. 3, pp. 860–868, 2016.

[15] B. Nagarajan, Z. Hu, X. Song, W. Zhai, and J. Wei, "Development of Micro Selective Laser Melting: The State of the Art and Future Perspectives," *Engineering*, vol. 5, no. 4, pp. 702–720, 2019.

[16] C. Pauzon, E. Hryha, P. Forêt, and L. Nyborg, "Effect of argon and nitrogen atmospheres on the properties of stainless steel 316 L parts produced by laser-powder bed fusion," *Mater. Des.*, vol. 179, p. 107873, Oct. 2019.

[17] Z. Li *et al.*, "Tensile properties, strain rate sensitivity, and activation volume of additively manufactured 316L stainless steels," *Int. J. Plast.*, vol. 120, pp. 395–410, 2019.

[18] U. Scipioni Bertoli, B. E. MacDonald, and J. M. Schoenung, "Stability of cellular microstructure in laser powder bed fusion of 316L stainless steel," *Mater. Sci. Eng. A*, vol. 739, pp. 109–117, 2019.

[19] U. Scipioni Bertoli, B. E. MacDonald, and J. M. Schoenung, "Stability of cellular microstructure in laser powder bed fusion of 316L stainless steel," *Mater. Sci. Eng. A*, vol. 739, no. August 2018, pp. 109–117, 2019.

[20] Google, "Google trends resuls for 'Machine learning,'" 2020. .

[21] Wikipedia, "Machine Learning," *Wikipedia*, 2020. .

[22] D. E. Rumelhart, G. E. Hinton, and R. J. Williams, "Learning representations by back-propagating errors," *Nature*, vol. 323, no. 6088, pp. 533–536, 1986.

[23] B. L. Decost and E. A. Holm, "A computer vision approach for automated analysis and classification of microstructural image data," *Comput. Mater. Sci.*, 2015.

[24] S. Lee, J. Peng, A. Williams, and D. Shin, "ASCENDS: Advanced data SCiENce toolkit for Non-Data Scientists," *J. Open Source Softw.*, vol. 5, no. 46, p. 1656, Feb. 2020.

[25] B. Wattrisse, A. Chrysochoos, J. M. Muracciole, and M. Némoz-Gaillard, "Analysis of strain localization during tensile tests by digital image correlation," *Exp. Mech.*, vol. 41, no. 1, pp. 29–39, 2001.

[26] ASTM, "ASTM E112-13: Standard test methods for determining average grain size," *ASTM Int.*, pp. 1–28, 2013.

[27] Oxford Instruments, "EBSD Explained," *EBSD Explain.*, pp. 1–23, 2015.

[28] "Black Glass Filled Epoxy Powder Cure Schedule.pdf." Allied High Tech, p. 1, 2020.

[29] T. R. Smith, J. D. Sugar, C. San Marchi, and J. M. Schoenung, "Strengthening mechanisms in directed energy deposited austenitic stainless steel," *Acta Mater.*, vol. 164, pp. 728–740, Feb. 2019.

[30] J. Yu, M. Rombouts, and G. Maes, "Cracking behavior and mechanical properties of austenitic stainless steel parts produced by laser metal deposition," *Mater. Des.*, vol. 45, pp. 228–235, 2013.

[31] J. Schindelin *et al.*, “Fiji: an open-source platform for biological-image analysis,” *Nat. Methods*, vol. 9, no. 7, pp. 676–682, 2012.

[32] M. A. Stephens, “EDF statistics for goodness of fit and some comparisons,” *J. Am. Stat. Assoc.*, vol. 69, no. 347, pp. 730–737, 1974.

[33] E. Ramirez-Cedillo *et al.*, “Process planning of L-PBF of AISI 316L for improving surface quality and relating part integrity with microstructural characteristics,” *Surf. Coatings Technol.*, vol. 186, p. 125956, May 2020.